1

Nonparametric Data Analysis Methods in Medical Imaging

Daniel E. Osborne [1], Vic Patrangenaru[2], Mingfei Qiu[2] and Hilary W. Thompson[3]

[1] *Department of Mathematics, Florida Agricultural & Mechanical University, Tallahassee, FL*
[2] *Department of Statistics, Florida State University, Tallahassee, FL*
[3] *School of Medicine, Division of Biostatistics, Louisiana State University, New Orleans, LA*

1.1 Introduction

Shape based statistical methods for medical imaging started around the early nineties (see Bookstein (1991), Dryden and Mardia (1998)) and the first nonparametric methods started being used slightly later. A classical medical imaging library that was heavily used in developing nonparametric tests in medical imaging was the one resulting from the Louisiana Experimental Glaucoma Study (LEGS), consisting of two types of imaging outputs: Heidelberg Retina Tomograph (HRT) images, and stereo pairs of images of the back of the eye (see Burgoyne et al. (2000)). The LEGS images are from Rhesus monkeys retinae. Tragically, the animals survived all the experiments, only to fall victims of the hurricane Katrina in 2005. In each of the individuals in the LEG study, an increased internal ocular pressure (IOP) was induced in one eye, while the other eye was left as control. Both eyes were imaged, and for each individual in the study, a complete set of observations, both HRT and stereo pairs were stored. The stereo pairs consisting in four optic nerve head (ONH) images were processed only in 2008 or later. They consisted in two images of the control eye (A) and two of the treated eye (B). Section 1.2 is dedicated to a review of results of nonparametric shape data analysis for HRT and stereo LEGS library data. HRT image data allows a recovery of the similarity shape information, therefore, for such data, the analysis is performed on the space Σ_3^k of direct similarity shapes of k-ads in 3D , known as *Kendall shape space* . Along these lines, we recall results from Derado et al. (2004) and from Bhattacharya and Patrangenaru (2005). For the stereo LEGS data, the camera parameters are unknown, thus only 3D projective shape data could be recovered. A 3D projective shape change analysis due to Crane and Patrangenaru (2011) is therefore pursued in this part of section 1.2.
In Section 1.3 we focus on the important task of recovery of 3D data from CT scans of the human skull. This task includes pre-processing and post-processing steps for CT images. The pre-processing step consists of the extraction the boundary of the bone structure from the CT slices while the post-processing step consists of 3D reconstruction of the virtual skull from these bone extractions. Given that the bilateral symmetry of the skulls

allows for a 3D size-and-reflection shape analysis on a manifold, therefore in Section 1.4, we briefly introduce the general nonparametric bootstrap on manifolds methodology, based on extrinsic means and extrinsic sample covariance matrices computations. Next, in Section 1.5 we introduce in detail the 3D size-and-reflection shape space $SR\Sigma^k_{3,0}$, as orbifold (space of orbits of the action of the orthogonal group $O(3)$ on centered k-ads in general position in $\mathbb{R}^3$. The Schoenberg embedding, the Schoenberg extrinsic mean, and the asymptotic behavior of the Schoenberg sample mean are also given in this section, for which the main reference is Bandulasiri et al. (2009). In Section 1.6 we present preliminary results for skull shape analysis based on bootstrap distributions of the Schoenberg's sample mean size-and-reflection shape for a selected group of k anatomical landmarks, and report a confidence region for the Schoenberg mean configuration of the corresponding k-ads on the midface.
The third part of the paper is dedicated to examples of nonparametric analysis on homogeneous spaces applied to MRI brain imaging. The first example, following results from Osborne et al. (2013) is given in Section 1.7. There a two sample test for DTI intrinsic means, based on their nonparametric methodology was applied to a concrete DTI small data set previously analyzed by Schwartzman et al. (2008), consisting of a voxelwise comparison of spatially registered DT images belonging to two groups of children, one with normal reading abilities and one with a diagnosis of dyslexia. The data provides strong evidence of differences between the intrinsic means of the two groups. The second example, in Section 1.8 is on the infinitely dimensional homogeneous space of direct similarity shape of contours, in the context of neighborhood hypothesis testing on manifolds, as it was recently developed in Ellingson et al. (2013). As an illustrative application, a test is carried out to see how far is the average direct similarity shape of contours of the mid section of corpus callosum in elderly people from Albert Einstein's, at the time when he just passed away.

1.2 Shape analysis of the Optic Nerve Head

Since glaucoma is a disease affecting the 3D appearance of the ONH region due to high IOP, it leads to a change in the 3D shape of this region. Given the small sample size of the LEGS data, any analysis has to undergo a drastic dimension reduction. For shape data, a first step in the dimension reduction consists in a selection of a few significant anatomical landmarks. In the case of HRT outputs, each "image" was presented in the form of a series of 256×256 2D arrays of ONH height values from a plane spanned by the ridge of the ONH cup. Due to the increased IOP, as the soft spot where the ONH enters the eye is pushed backwards, eventually, the optic nerve fibers that spread out over the retina to connect to photoreceptors and other retinal neurons can be compressed and be damaged. Two processed images of the ONH cup surface before and after the IOP increment are shown in Figure 1.1.

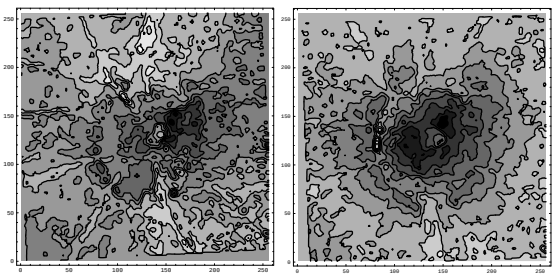

Figure 1.1 Change in the ONH topography from normal (left) to glaucomatous (right)

Regarding landmark based dimension reduction analysis, assume the position vectors of these landmarks are $X_1, \ldots, X_k, k \geq 4$. Two configurations of landmarks have the same *Kendall shape*, if they can be superimposed after a direct similarity. The *Kendall shape* of the configuration $x = (x_1, \ldots, x_k)$ is labelled $o(x)$ and the space Σ_m^k, of shapes of configurations of k points in $\mathbb{R}^m$ at least two of which are distinct introduced in Kendall (1984) is the *Kendall shape space* of k-ads in m dimensions.
We now return to the shape of an ONH region, which resembles a "cup" in the shape of half an ellipsoid with an ellipse shaped margin. Following Patrangenaru et al. (2000), in Bhattacharya and Patrangenaru (2005) four landmarks were used; the first three, denoted by S, T, and N were chosen to be the "top, left and right" points on this ellipse, i.e. (when referring to the left eye) Superior, Templar and Nose papilla (see Derado et al. (2004)). The fourth landmark, V, was called *vertex*, the deepest point inside the ellipse bordering the ONH cup; therefore, in

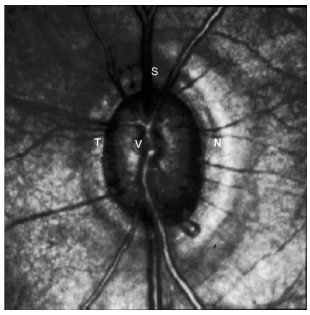

Figure 1.2 Landmarks on the ONH for HRT outputs

Bhattacharya and Patrangenaru (2005) the data analysis was carried out on the shape space of tetrads, Σ_3^4, which is topologically a 5 dimensional nonstandard sphere, according to Kendall et al. (1999), pp.33. On the other hand, it is known that if a probability distribution on Σ_m^k has small support outside a set of singular points, any distance that is compatible with the orbifold topology considered is not relevant in data analysis (Dryden and Mardia (1998), p.65) as the data can be linearized. Therefore for practical considerations, distances that are derived using a partition of unity and Euclidean distances in various coordinate domains of Σ_3^4 are useful for such distributions. In Dryden and Mardia (1998), pp.78-80, five coordinates, that were called later called *DM coordinates* by Bhattacharya and Patrangenaru (2005), were defined on the generic subset of Kendall shapes of nondegenerate tetrads in Σ_3^4, and labeled $v^1, \ldots, v^5$. The five DM coordinates proved useful in detecting a significant glaucomatous means shape "difference" due to increase IOP, as shown in Bhattacharya and Patrangenaru (2005). Nevertheless, since it was preferable to have a single medical measurement to detect glaucoma from HRT outputs, Derado et al. (2004) defined a *glaucoma index*, and showed that this index is useful in mean shape change detection. Due to its simplicity, the landmark based glaucoma index method, is cited in the medical literature (see Hawker et al. (2007), Sanfilippo et al. (2009)).

In the case of stereo data of the back of the eye, which is the most common imaging data for eye disease detection, Crane and Patrangenaru (2011) developed a landmark based projective shape analysis approach. They analyzed data from LEGS consisting of fifteen independent complete paired observations of stereo pairs. Figure 1.3 displays the fifteen independent stereo pairs of observations. Unlike with HRT data, which is 3D from the outset, in the case of stereo imaging, one has to retrieve the 3D structure of the landmarks configuration from

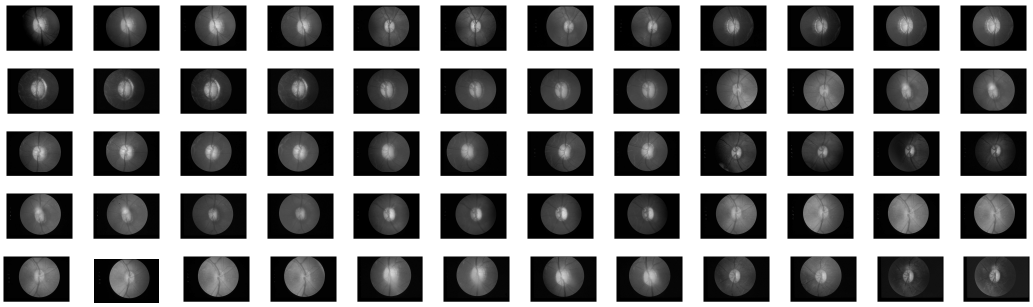

Figure 1.3 Optic Nerve Head region data

its stereo pair images. The problem of reconstruction of a 3D configuration of points from a pair of its *ideal noncalibrated camera* images was solved by Faugeras (1992) and Hartley et al. (1992), who showed that:

Theorem 1.2.1 *A finite configuration $\mathcal{C}$ of eight or more points in general position in 3D can be reconstructed from the coordinates of the images of these points in two ideal noncalibrated digital camera views, and the reconstruction $\mathcal{R}$ is unique up to a projective transformation in 3D.*

This projective ambiguity in Theorem 1.2.1 was reinterpreted in Sughatadasa (2006), Patrangenaru et al. (2010), Crane and Patrangenaru (2011) as follows

Corollary 1.2.2 *The projective shapes of the 3D configurations of points $\mathcal{R}$ and $\mathcal{C}$ in Theorem 1.2.1 are identical.*

Among reconstruction algorithms, Crane and Patrangenaru (2011) suggested using the eight point algorithm in Ma et al. (2006) (p. 121), for a conveniently selected camera internal parameters matrix, or the refined eight point algorithms for the estimate of the fundamental matrix (Ma et al. (2006), p. 188, p. 395), (Hartley and Zisserman (2004), p.282). For details on the reconstruction of the projective shape of a 3D configuration from the pixel coordinates of two of its digital images, see Patrangenaru et al. (2010) and the references therein. In Crane and Patrangenaru (2011) coordinates of nine landmarks on the approximate elliptic contour of the ridge of the ONH were recorded, as well as those of certain blood vessels junctions and estimated location of the deepest points. These included the landmarks considered for HRT data. They were S(superior), I(inferior), N(nasal), T(templar), V(vertex-the deepest point of the ONH cup), SM(mid-superior), IM(mid-inferior), NM(mid-nasal) and TM(mid-templar), and their positions in the ONH cup are schematically displayed in the Figure 1.4. Note that projective shape analysis can be performed using different approaches, by representing a projective shape on a certain projective shape space. The most recent approach, due to Kent and Mardia (2012) has the advantage of being independent of the landmarks labels. On the other hand, the projective frame approach (Mardia and Patrangenaru (2005), Patrangenaru et al. (2010)) has the advantage of being rooted in projective geometry and computationally faster; no 3D projective shape analysis was so far published using the approach in Kent and Mardia (2012). Moreover in 3D, the projective shape space obtained via the projective frame approach has a Lie group structure, thus allowing a two sample test for mean projective shape change in matched pairs to be reduced to a one sample test. For such reasons, in their projective shape analysis of mean glaucomatous projective shape change, Crane and Patrangenaru (2011) used a projective frame approach, by selecting the projective frame $\pi = (N, T, S, I, V)$. For the analysis, the projective coordinates (defined in Mardia and Patrangenaru (2005)) of the remaining four landmarks $[h_{1,ji}], [h_{2,ji}], [h_{3,ji}], [h_{4,ji}], j = 1, 2, i = 1, \ldots, 15$ were computed with respect to this frame. To test if there is a difference between the extrinsic mean projective shape change from the configuration in the control eye and the treated eye, given the small size of the sample Crane and Patrangenaru (2011) computed the bootstrap statistics $T_s^*, s = 1, 2, 3, 4$, in Patrangenaru et al. (2010) for the four $\mathbb{R}P^3$ marginals for $20,000$ resamples. The

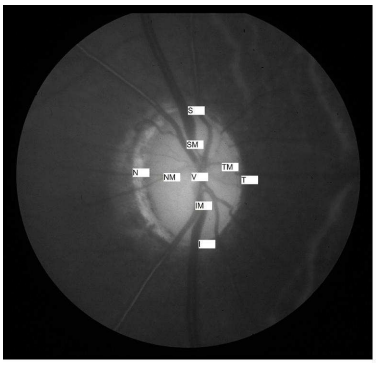

Figure 1.4 Nine anatomical landmarks of the ONH for one stereo image

histograms for the bootstrap distributions of $T_s^*, s = 1, 2, 3, 4$ corresponding to the marginal axes are displayed in Figure 1.5 (see also Crane and Patrangenaru (2011)). The values of the statistics $T_s, s = 1, 2, 3, 4$ under the null

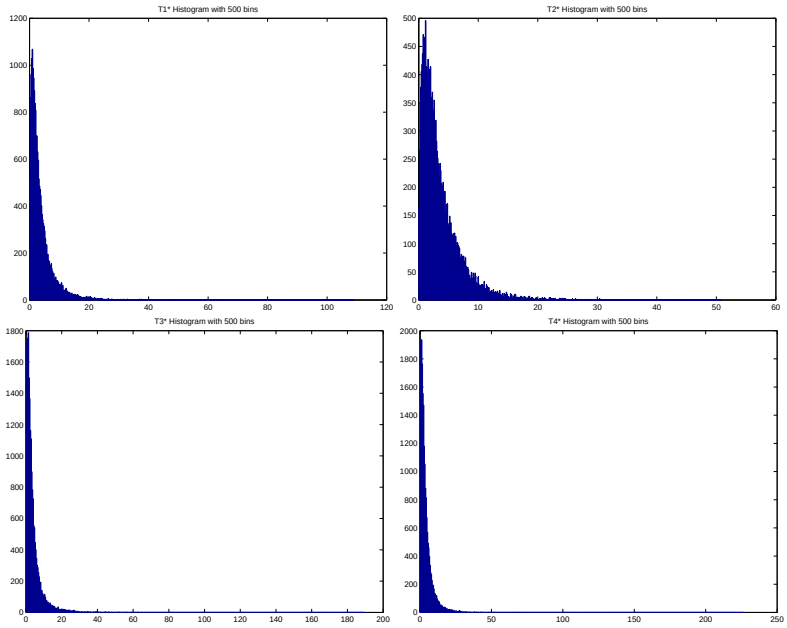

Figure 1.5 Histograms for the bootstrap distributions of $T_s^*, s = 1, 2, 3, 4$ for 20,000 resamples.

hypothesis of *no projective shape change* are :
$T_1 = 1474.7, T_2 = 2619.9, T_3 = 860.2, T_4 = 1145.7$, and since the T_1, T_2, T_3 and T_4 are much larger than the corresponding cutoffs given above, there is a significant mean projective shape change due to the increased IOP in the treated eye.
It is worth noting that while tests statistics for mean glaucomatous Kendall shape change based on HRT outputs, including tests for mean glaucoma index change in Derado et al. (2004) are easier to compute, most ophthalmologists cannot afford an HRT, while any ophthalmologist has access to stereo cameras designed for eye fundus imagery; thus tests for mean projective shape change due to glaucoma onset might be more useful for onset of glaucoma detection.

1.3 Extraction of 3D data from CT scans

In this section, our main focus is on preprocessing and post-processing steps of CT images.

1.3.1 CT Data Acquisition

The CT images were taken using a computed tomography device (CT scanner). This was done for twenty-eight individuals. A computed tomography (CT) scan uses X-rays to make detailed pictures of structures inside of the body. A CT scan is used to study all parts of the human body. In this study, one CT scan in our data set consists of about 100+ X-rays of the head above the mandible per individual. Figure 1.6 displays an example of one CT scan of an individual in our data set.

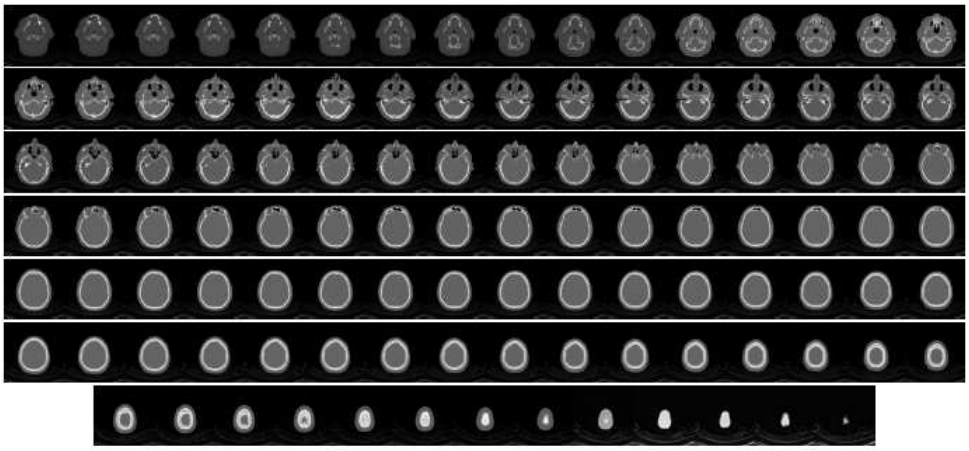

Figure 1.6 CT Scan of an Individual

1.3.2 Object Extraction

Numerous methods of thresholding and segmentation have been developed for object extraction from 2D for 3D display Harris and Camp (1984), Robb (1996), Serra et al. (1997), Sher (1977). Surface rendering (Gibson et al. (1998), Heffernan and Robb (1985), Herman and Liu (1977), Lorensen and Cline (1987), and Robb (1994)) and volume rendering (Cabra et al. (1994), Drebin et al. (1988), Kaufman et al. (1993), Levoy (1988), Pflesser et al. (1998), Robb (1994), and Robb and Barillot (1989)) are two different techniques that have traditionally enabled the visualization of 3D biomedical volume data (images). Both techniques produce a visualization of selected structures in 3D volume data (images), but one should note that the methods involved in these techniques are quite different, and each has its advantages and disadvantages. Selection between these two approaches is often based on the particular nature of the biomedical image data, the application to which the visualization is being applied, the desired result of the visualization, and computational resources. Here we focus on surface rendering techniques. Surface rendering, when based on a sequence of stacked 2D images, requires the extraction of contours (the edge of the intersection of the object with each slice, in our case of 2D slice level the skull surface). Then a tiling algorithm is applied that places surface patches (or tiles) at each contour point and with hidden surface removal and shading, the surface is rendered visible. The advantage of this technique lies in the relatively small amount of contour data, resulting in a fast 3D rendering (reconstruction) speeds. The disadvantages may vary depending on object extraction (or segmentation) software or algorithms. Ideally, one would like to extract all objects of

interest from 3D volume data (images) quickly and accurately. In other words, the extracted object should be a good representation of the original object inside of the image. Here we explored various segmentation methods in order to extract the bone structure from the CT slices and then perform 3D reconstruction of the virtual skull from these bone extractions.

Segmentation: Minimizing the Geodesic Active Contour

Segmentation is a well studied area and it is usually formulated as the minimization of a cost/energy function subjected to some constraints. Segmenting 3D image volumes slice by slice using image processing techniques is a lengthy process and requires a post-processing step to connect the sequence of 2D contours into a continuous surface (3D reconstruction). Caselles et al. (1997) introduced the Geodesic Active Contour (GAC) algorithm, as an enhanced version of the snake model of (Kass et al. (1988)). The GAC algorithm is defined as the following variation problem:

$$\min_{C} \{E_{GAC}[C]\}, \text{ where } E_{GAC}[C] = \int_0^{|C|} g(|\nabla I(C(s))|)dl. \tag{1.3.1}$$

In (1.3.1) $|C|$ is the Euclidean length of the curve C and dl the Euclidean element of arc. The edge detection function, $g \in (0, 1]$ in Eq. 1.3.1 has the following meanings: values close to 0 are at strong edges in the image I whereas, values close to 1 are not at edges in the image I. $|\nabla I|$ acts as a edge detector. In particular, ∇I is the gradient of the gray level along the curve $C(s)$ Caselles et al. (1997). A (local) minimal distance path between given points is a geodesic curve. To show this (Caselles et al. (1997)) used the classical Maupertuis principle from dynamical systems (Caselles et al. 1997) which essentially explains when an energy minimization problem is equivalent to finding a geodesic curve in a Riemannian space (see also Milnor (1963)). Typically, to find the global optimal solution of equation 1.3.1, graph based approaches are commonly used which rely on partitioning of a graph that is built based on the image I. Unfortunately, such approaches can lead to major systematic discretization error problems. Appleton and Talbot (2006) presented an approach that minimizes the GAC energy using continuous maximal flows. The amazing gain from their approach is that it does not suffer from any discretization errors. Bresson et al. (2005) produced a different approach, which uses the *weighted Total Variation*. The *weighted Total Variation* or simply *weighted TV* is defined as

$$TV_g(u) = \int_\Omega g(x)|\nabla u|dx. \tag{1.3.2}$$

$TV_g(u)$ is the weighted gradient of u. The active contour C is a level-set of a function $u : [0, a] \times [0, b] \to \mathbb{R}$. In other words, u is an implicit representation of the active curve C, since C coincides with the set of points u = constant. Bresson et al. showed that under certain conditions, namely if u is a characteristic function 1_C then Eq. (1.3.2) is equivalent to E_{GAC} in (1.3.1). The details are provided in Bresson et al. (2005). In order to find the geodesic curve, the corresponding steepest-descent flow of Eq. (1.3.2) is computed. If we allowed u to vary continuously in $[0, 1]$, then Eq. (1.3.2) becomes a convex function, meaning that one can compute the global minimizer of it. Unger et al. (2008) proposed the following variational image segmentation algorithm:

$$\min_{u\in[0,1]} \{E_{Seg}\} \text{ where } E_{Seg} = \int_\Omega g(x)|\nabla u|d\Omega + \int_\Omega \lambda(x)|u - f|d\Omega. \tag{1.3.3}$$

Here the first term of the energy is the *weighted TV* of u as defined in Eq. (1.3.2), which minimizes the GAC energy. The second term is used to incorporate constraints into the energy function. The variable $f \in [0, 1]$ is provided by the user and it indicates foreground $(f = 1)$ and background $(f = 0)$ seed regions. The spatially varying parameter $\lambda(x)$ is responsible for the interpretation of the information contained in f. Figure 1.7 displays ten 3D reconstruction based on the method of Unger et al. (2008) summarized above.

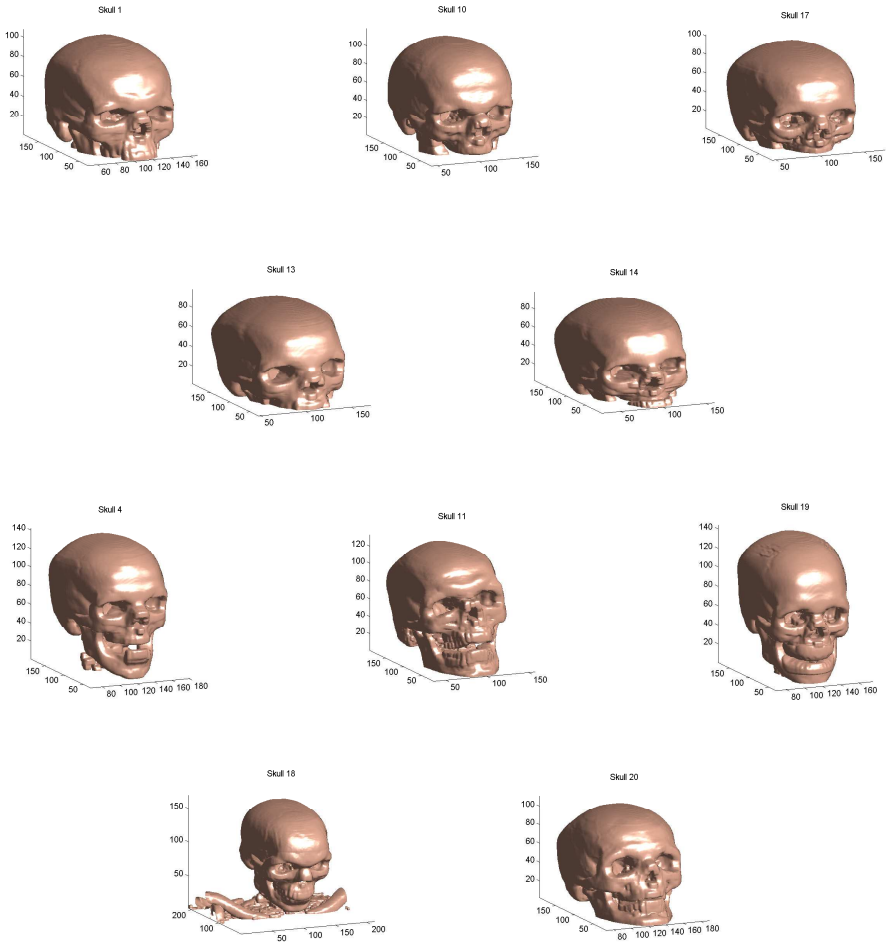

Figure 1.7 Select 3D Reconstruction Results via segmentation

1.4 Means on Manifolds

1.4.1 Consistency of the Freć het sample mean

Consider a separable metric space $(\mathcal{M}, \rho)$ and a random object

$$X : (\Omega, \mathcal{A}, \mathbb{P}) \to (\mathcal{M}, \mathcal{B}_\rho), \tag{1.4.1}$$

Given a probability measure Q associated with a random object X on a metric space $\mathcal{M}$ with the distance ρ, a natural index of location is the *Fréchet mean* (Fréchet (1948), Ziezold (1977)) which is the minimizer of

$$F(p) = E(\rho^2(p, X)) = \int \rho^2(p, x)Q(dx), \tag{1.4.2}$$

if the minimizer is unique. The set of all such minimizers form the *Fréchet mean set*. Bhattacharya and Patrangenaru (2005)) showed that if the Fréchet mean set has only one point (*Fréchet mean*), then the Fréchet sample mean (set) is a strongly consistent estimator of the Fréchet mean. In this paper, we define the definition of a distance between size-and-reflection shapes just like that presented in (Bandulasiri and Patrangenaru (2005) and Bandulasiri et al. (2009)). The Fréchet mean is called *extrinsic mean* if the distance ρ is induced by an embedding $j : M \to \mathbb{E}^N$, and *intrinsic mean* if the distance ρ is induced by a Riemannian structure on M. Furthermore, the

extrinsic (intrinsic) sample mean is a consistent estimator of the extrinsic (intrinsic) mean.
The *projection map* $P_j : F^c \to j(M)$ is defined as

$$P_j(p) = j(x) \text{ if } d_0(p, j(M)) = d_0(p, j(x)), \tag{1.4.3}$$

where d_0 is the Euclidean distance and F^c is the set of nonfocal points of M in $\mathbb{E}^N$. In Bhattacharya and Patrangenaru (2003) it was shown that if X is a j-nonfocal random object on $\mathcal{M}$, then the extrinsic mean is given by

$$\mu_j = j^{-1}(P_j(E(j(X)))), \tag{1.4.4}$$

where P_j is the projection on $j(M)$. Furthermore, if we let $X = (X_1, \ldots, X_n)$ be i.i.d. M-valued random variables with nonfocal measure Q on $(\mathcal{M}, j)$ and if the mean $\overline{j(X)}$ of the sample $j(X) = (j(X_1), \ldots, j(X_n))$ is a nonfocal point, then the *extrinsic sample mean* is given by

$$\overline{X}_j := j^{-1}\left(P_M(\overline{j(X)})\right). \tag{1.4.5}$$

The *extrinsic sample covariance matrix*, which shows in the *extrinsic* T^2 asymptotic statistics (see Bhattacharya and Patrangenaru (2005)), is

$$S_{j,E,n} = \left[\left[\sum d_{\overline{j(X)}}P_j(e_b) \cdot e_a(P_j(\overline{j(X)}))\right]_{a=1,\ldots,m}\right] \cdot S_{j,n} \cdot \left[\left[\sum d_{\overline{j(X)}}P_j(e_b) \cdot e_a(P_j(\overline{j(X)}))\right]_{a=1,\ldots,m}\right]^T, \tag{1.4.6}$$

where $S_{j,n} = n^{-1}\sum_{r=1}^N (j(X_r) - \overline{j(X)})(j(X_r) - \overline{j(X)})^T$ is the sample covariance and $(e_a(y), a = 1, \ldots, N)$ is an orthoframe field around $P_j(\overline{j(X)})$, whose first m vectors are in $T_y j(M), y \in j(M)$, and $d_{\overline{j(X)}}P_j$ is the differential of P_j at the sample mean $\overline{j(X)}$.

1.4.2 Nonparametric Bootstrap

Efron's nonparametric bootstrap methodology (Efron (1982)) is extremely useful in data analysis on manifolds where the sample is small. If $\{X_r\}_{r=1,\ldots,n}$ is a random sample from the unknown distribution Q, and $\{X_r^*\}_{r=1,\ldots,n}$ is a bootstrap resample from $\{X_r\}_{r=1,..,n}$, then $S^*_{j,E,n}$ is obtained from $S_{j,E,n}$ substituting $X_1^*, \ldots, X_n^*$ for $X_1, \ldots, X_n$. For example, if n is not large, from Bhattacharya and Patrangenaru (2005) it is known that a 100(1 - α)% nonparametric bootstrap confidence region , for the extrinsic mean μ_j is given by $D^*_{n,\alpha} := j^{-1}(V^*_{n,\alpha})$, where

$$V^*_{n,\alpha} = \{\mu \in j(\mathcal{M}) : n\|S^{-\frac{1}{2}}_{j,E,n} \tan_{P_j(\overline{j(X)})}(P_j(\overline{j(X)}) - P_j(\mu))\|^2 \leq d^*_{1-\alpha}\}. \tag{1.4.7}$$

Here $\tan_p(v)$ is the tangential component of v with respect to the splitting $T_v\mathbb{E}^N = T_vM \oplus (T_vM)^\perp$ and $d^*_{1-\alpha}$ is the upper $100(1-\alpha)\%$ point of the values

$$n\|{S^*_{j,E,n}}^{-\frac{1}{2}} \tan_{P_j(\overline{j(X^*)})}(P_j(\overline{j(X^*)}) - P_j(\overline{j(X)}))\|^2 \tag{1.4.8}$$

among the bootstrap resamples. This region has coverage error $O_p(n^{-2})$.

1.5 3D Size-and-Reflection Shape Manifold

1.5.1 Description of $SR\Sigma^k_{3,0}$

We consider configurations $\mathbf{x} = (x^1, \ldots, x^k)$ which consist of $k > 3$ labeled points in $3D$, called *k-ads*. These k-ads are in *general position* (i.e. the minimal affine subspace containing the landmarks in $\mathbf{x}$ spans $\mathbb{R}^3$) and they

represents k locations on an object. Translation is removed by centering the k-ad $\mathbf{x} = (x^1, \ldots, x^k)$ to

$$\xi = (\xi^1, \ldots, \xi^k), \xi^j = x^j - \overline{x}, \forall\ j = 1, \ldots, k. \tag{1.5.1}$$

The set of all centered k-ads form a vector subspace $L_k^3 \subset (\mathbb{R}^3)^k = M(3, k; \mathbb{R})$ of dimension $3k - 3$, where

$$L_k^3 = \{\xi \in M(3, k; \mathbb{R}), \xi \mathbf{1_k} = 0\}. \tag{1.5.2}$$

The orthogonal group $O(3)$ acts on L_k^3 on the left, via the action α given by $\alpha(A, \xi) = A\xi$. The *3D size-and-reflection shape* $[\mathbf{x}]_{RS}$ of a k-ad $\mathbf{x}$ is the $O(3)$-orbit of the corresponding centered configuration ξ under the diagonal action $\alpha_k(A, \xi) = (\mathbf{A}\xi^{\mathbf{1}}, \ldots, \mathbf{A}\xi^{\mathbf{k}})$ of the orthogonal group $O(3)$ on the set of all centered k-ads:

$$[\mathbf{x}]_{RS} = \{A\xi : A \in O(3)\} \tag{1.5.3}$$

A k-ad is in general position if and only if $\{\xi_1, \ldots, \xi_k\}$ spans $\mathbb{R}^3$. The *3D size-and-reflection shape space* $SR\Sigma_{3,0}^k$ is the set of all size-and-reflection shapes of k-ads in general position

$$SR\Sigma_{3,0}^k = \{[\mathbf{x}]_{RS},\ \ \text{rank}(\mathbf{x}) = 3\} \tag{1.5.4}$$

This space is a manifold because the action of an orthogonal matrix on $\mathbb{R}^3$ is uniquely determined by its action on a basis of $\mathbb{R}^3$, and a centered k-ad in general position includes such a basis (Bandulasiri and Patrangenaru (2005)). The dimension of $SR\Sigma_{3,0}^k$ is $3k - 6$. This space, $SR\Sigma_{3,0}^k$, can be represented as a quotient space $L_{k,0}^3 \backslash O_3 / O(3)$, where $L_{k,0}^3$ is given by (1.5.2).

1.5.2 Schoenberg embeddings of $SR\Sigma_{3,0}^k$

Bandulasiri and Patrangenaru (2005) introduced the Schoenberg embedding of reflection shapes in higher dimensions to perform an extrinsic analysis. The *Schoenberg embedding* of the size-and-reflection shape manifold is $J : SR\Sigma_{3,0}^k \to S(k, \mathbb{R})$, given by

$$J([\xi]_{RS}) = \xi^T \xi. \tag{1.5.5}$$

The range of the Schoenberg embedding of $SR\Sigma_{3,0}^k$ is the subset $SM_{k,3}$ of $k \times k$ positive semidefinite symmetric matrices A with $rank(A) = 3,\ A\mathbf{1_k} = \mathbf{0}$. Also M_k is the space of $k \times k$ symmetric matrices A with $A\mathbf{1_k} = \mathbf{0}$. Dryden et al. (2008) and Bandulasiri et al. (2009) showed that if the map ϕ from M_k to $S(k-1, \mathbb{R})$, given by $\phi(A) = HAH^T$, where $(1_k, H^T) \in O(k)$, is an isometry, then $\psi : S\Sigma_{3,0}^k \to S(k-1, \mathbb{R})$, given by

$$\psi([\mathbf{x}]_{RS}) = H\xi^{\mathbf{T}}\xi H^T, \tag{1.5.6}$$

is an embedding; the Schoenberg embedding and the embedding ψ induce the same distance on $SR\Sigma_{3,0}^k$.

1.5.3 Schoenberg Extrinsic Mean on $SR\Sigma_{3,0}^k$

Let $\mathbf{X}$ be a random k-ad in general position which is centered as $\mathbf{X_0} = (X^1 - \overline{X}, \ldots, X^k - \overline{X}) \in (\mathbb{R}^3)^k \simeq M(3, k; \mathbb{R})$.

Theorem 1.5.1 *(Bandulasiri et al. (2009))* *Assume $C = \sum_{i=1}^k \lambda_i e_i e_i^T$ is the spectral decomposition of $C = E(\mathbf{X_0}\mathbf{X_0}^T)$, and $v_j = \sqrt{\lambda_j} e_j, j = 1, \ldots, k$. Obviously $C1_k = 0, C \geq 0$. Let $\xi = V^T$, where*

$$V = (v_1 v_2 v_3). \tag{1.5.7}$$

Then the extrinsic mean μ_J size-and-reflection shape exists if $\lambda_3 > \lambda_4$ and $\mu_J = [\xi]_{RS}$.

Furthermore, if $k = 4$, then the projection P_ψ is the identity map, and any distribution Q is ψ-nonfocal and $\psi(\mu_S)$ is the mean μ of $\psi(Q)$. The approach taken in Theorem 1.5.1 is the same as saying that, given C, ξ is a classical solution in $\mathbb{R}^3$ to the MDS problem, as given in Mardia et al. (1979) in terms of the 3 largest eigenvalues of C.

For estimation purposes, let $\{\mathbf{x}_1, \ldots, \mathbf{x}_n\}$ be a sample of k-ads in general position in $\mathbb{R}^3$, where $\mathbf{x}_j = (x_j^1, \ldots, x_j^k)$, for $j = 1, \ldots, n$. The *extrinsic sample mean size-and-reflection shape* is $\overline{[\mathbf{x}]}_E = [\hat{\xi}]_{RS}$, where $\hat{\xi}$ is given by the eigenvectors corresponding to the 3 largest eigenvectors of

$$\hat{C} = \frac{1}{n} \sum_{j=1}^{n} \xi_j^T \, \xi_j \tag{1.5.8}$$

assuming that $\hat{\lambda}_3 > \hat{\lambda}_4$, where $\hat{\lambda}_1 \geq \cdots \geq \hat{\lambda}_k$ are the eigenvalues of $\hat{C}$. $\hat{\xi}$ is the classical solution in $\mathbb{R}^3$ to the MDS problem (Mardia et al. (1979), p. 397) for the matrix $\hat{C}$. Note that ξ_j is the matrix obtained from $\mathbf{x}_j$ after centering (removing translation). If $\lambda_3 > \lambda_4$, then $\mu_J = [\mu]_{RS}$, and $[\hat{\mu}_{MDS}]_{RS}$ (see Bandulasiri et al. (2009)) is a consistent estimator of $[\mu]_{RS}$. The asymptotic distribution of the extrinsic sample mean size-and-reflection shape is given in Bandulasiri et al. (2009).
Related results are given in Dryden et al. (2008) and Kent (1994).

1.6 3D Size-and-Reflection Shape Analysis of the Human Skull

Here we give a comprehensive application of size-and-reflection shape space $SR\Sigma_{3,0}^k$ of k-ads in general position in 3D. One potential application is to surgery planning, where a natural approach is to take into account size in addition to shape when analyzing the CT scan data. In this context, one performs a nonparametric analysis on the 3D data retrieved from CT scans of adults, on the on size-and-reflection shape space $SR\Sigma_{3,0}^k$ of k-ads in general position in 3D.

1.6.1 Confidence Regions for 3D mean Size-and-Reflection Shape Landmark Configurations

Once we obtained the 3D reconstruction of the virtual skull from the bone extractions, we proceed to perform landmark based analysis based on the Schoenberg embedding. For the purpose of one analysis we were interested in $k = 9$ and $k = 17$ matched landmarks around the eyes. The landmarks were registered on the reconstructed 3D virtual skulls.

Here we consider nonparametric statistical analysis size-and-reflection shape data using landmarks in which each observation $\mathbf{x} = (x^1, \ldots, x^9)$ and $\mathbf{x} = (x^1, \ldots, x^{17})$ consists of 9 points and 17 points in $\mathbb{R}^3$ (See Figure 1.8). The landmark coordinates can be found in Appendix A and Appendix B of Osborne (2012), pages 74-77 and 78-84, respectively.

We remove translation by centering the k-ads $\mathbf{x} = (x^1, \ldots, x^9)$ and $\mathbf{x} = (x^1, \ldots, x^{17})$ to

$$\xi = (\xi^1, \ldots, \xi^9) \text{ and } \xi = (\xi^1, \ldots, \xi^{17})$$
$$\xi^j = x^j - \overline{x}, \forall\, j = 1, \ldots, 9 \text{ and } j = 1, \ldots, 17.$$

The set of these centered k-ads lie in the vector subspace $L_9^3 \in (\mathbb{R}^3)^9$ and $L_{17}^3 \in (\mathbb{R}^3)^{17}$, respectively. The dimensions of the manifolds $SR\Sigma_{3,0}^9$ and $SR\Sigma_{3,0}^{17}$ are $3k - 6$, where $k = 9$, respectively $k = 17$.

Finally, in order to estimate the 3D size-and-reflection shape for the selected group of landmarks, we compute the Schoenberg sample means. That is, we used 500 bootstrap resamples based on the original 20 skull configurations ($k = 9$ and $k = 17$), represented by the 3 by k matrices (where k was the number of landmarks selected in the analysis). For the purpose of one analysis we were interested in $k = 9$ and $k = 17$ landmarks

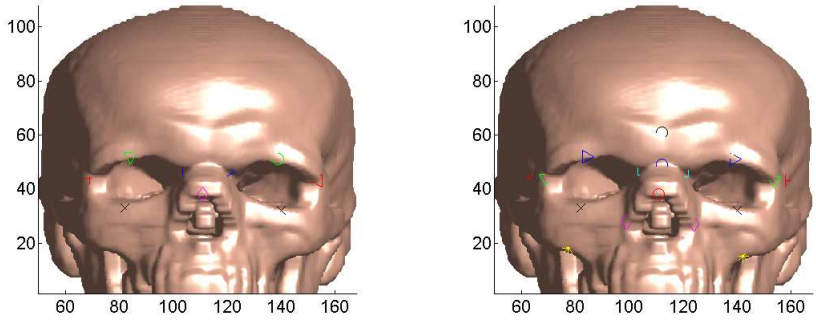

Figure 1.8 Two groups of landmarks around the eye: Right image has $k = 9$ and the left image has $k = 17$

around the eyes region. Registered representations, for these mean size-and-reflection shapes yield the bootstrap mean size-and-reflection shape configurations given in Figure 1.9 and Figure 1.10.

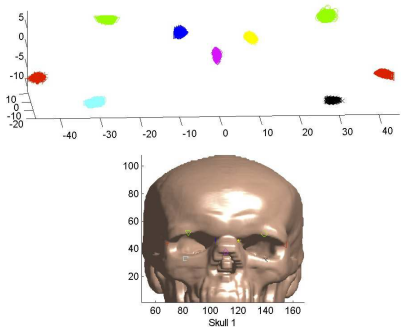

Figure 1.9 Bootstrap distribution for the Schoenberg sample mean configurations $k = 9$ based on 500 resamples

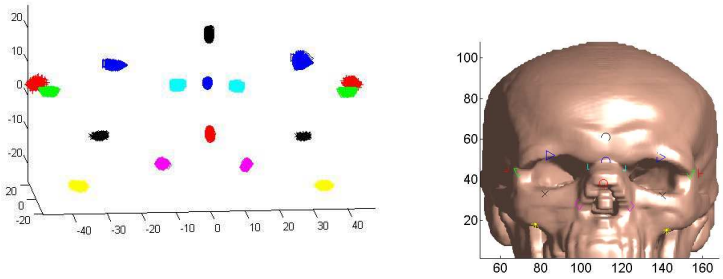

Figure 1.10 Bootstrap distribution for the Schoenberg sample mean configurations $k = 17$ based on 500 resamples

In addition, we provide a 90% simultaneous confidence limits for the 3D mean size-and-reflection shape configuration are given in Tables 1.1 and 1.2. Similar tables, with 90% simultaneous confidence bounds for the 3D mean size-and-reflection shape configuration of 17 landmarks given in Figure 1.8, based on the nonparametric bootstrap distribution displayed in Figure 1.10, are given in Osborne (2012). For practical purposes, these simultaneous confidence regions may be used for example to design helmets or other protection devices of the midface area region of an average individual.

Table 1.1 90% Lower Confidence Limit for the Bootstrap Distribution of the 3D Sample Mean Size-and-Reflection Shape Configuration.

Landmark	1	2	3	4	5	6	7	8	9
x	−45.76	−28.65	−9.75	−32.06	−0.90	7.84	27.15	40.79	26.28
y	10.10	−2.37	−5.91	0.27	−19.20	-3.84	0.86	10.04	−0.06
z	−0.19	9.73	4.24	−11.67	−8.06	3.00	−12.70	−1.70	9.36

Table 1.2 90% Upper Confidence Limit for the Bootstrap Distribution of the 3D Sample Mean Size-and-Reflection Shape Configuration.

Landmark	1	2	3	4	5	6	7	8	9
x	−42.03	−24.44	−7.27	−28.29	0.41	10.19	30.65	44.52	30.30
y	11.85	−0.93	−3.39	1.82	−15.92	−1.69	2.52	12.83	4.17
z	1.43	11.12	5.93	−10.02	−5.73	4.83	−11.25	−0.32	13.08

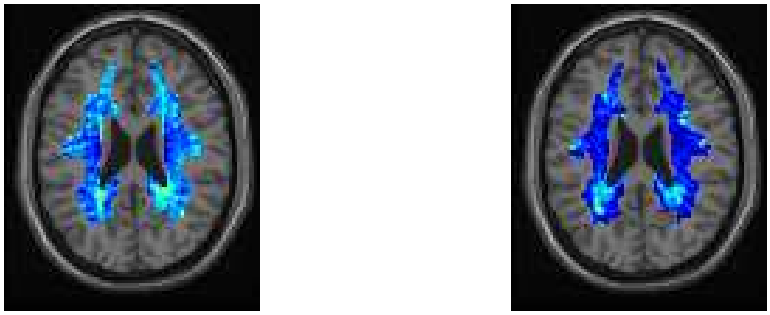

Figure 1.11 DTI slice images of a control subject (left) and of a dyslexia subject (right).

1.7 DTI data analysis

In this section, we analyze the Diffusion Tensor Images (DTI) data according to the new methodology presented in Osborne et al. (2013) using a concrete DTI example. The data was collected from two groups of children, a group of 6 children with normal reading abilities and a group of 6 children with a diagnosis of dyslexia. Twelve spatially registered diffusion MRIs (DT images) were obtained from the two groups of children, respectively. The prognosis is generally helpful for individuals whose dyslexia is identified early, who have supportive family and friends and a strong self-image, and who are involved in a proper remediation program. In Figure 1.11, we display DTI slices including a given voxel recorded in a control subject and a dyslexia subject.

Commonly in DTI group studies, a typical statistical problem is to find regions of the brain whose anatomical characteristics differ between two groups of subjects. Typically, the analysis consists of registering the DT images to a common template so that each voxel corresponds to the same anatomical structure in all the images, and then applying two-sample tests at each voxel.

Osborne et al. (2013) presented a nonparametric analysis of a single voxel at the intersection of the corpus callosum and corona radiata in the frontal left hemisphere that was found in Schwartzman et al. (2008) to exhibit the strongest difference between the two groups. Table 1 in Osborne et al. (2013) shows the data at this voxel for all 12 subjects. The d_{ij} in the table are the entries of the DT on and above the diagonal (the below-diagonal entries would be same since the DTs are symmetric).

For this analysis, the primary goal is to demonstrate that the nonparametric two-sample testing procedure in Section 3 of Osborne et al. (2013) is able to detect a significant difference between of the generalized Frobenius means of the clinically normal and dyslexia groups without increasing the dimensionality in the process. For distances, other than Riemannian ones, on the set $Sym^{+}(3)$ of 3×3 positive definite matrices, see Dryden et

al. (2009). Namely, we are interested in detecting, on average, from Diffusion Tensor Images (DTI), dyslexia in young children compared to their clinically normal peers, *without making any distributional assumptions*.
Given two independent populations with i.i.d. samples of random SPD matrices $X_{1,1}, X_{1,2}, \ldots, X_{1,n_1} \in Sym^+(3)$ from the clinically normal population and $X_{2,1}, X_{2,2}, \ldots, X_{2,n_2} \in Sym^+(3)$ from the dyslexia population with sample sizes of $n_1 = 6$ and $n_2 = 6$ and the total sample size $n = n_1 + n_2 = 12$, where, for $a = 1, 2, X_{a,1} \sim \mu_{F,a}$, the sample generalized Frobenius mean for the clinically normal population and dyslexia population is given by

$$\bar{x}_{1,F} = \begin{pmatrix} 0.6318 & 0.0046 & -0.0924 \\ 0.0046 & 0.9863 & -0.0873 \\ -0.0924 & -0.0873 & 0.7803 \end{pmatrix} \text{ and } \bar{x}_{2,F} = \begin{pmatrix} 0.6146 & -0.0261 & -0.1910 \\ -0.0261 & 0.8118 & -0.0901 \\ -0.1910 & -0.0901 & 0.9537 \end{pmatrix}.$$

The test statistics $\hat{T}$ and V, previously described in Osborne et al. (2013), are given by

$$\hat{T} = \begin{pmatrix} 0.9862 & 0.0000 & 0.0000 \\ -0.0485 & 0.9067 & 0.0000 \\ -0.1487 & -0.0152 & 1.0781 \end{pmatrix} \text{ and } V = \begin{pmatrix} -0.0139 & 0.0000 & 0.0000 \\ -0.0513 & -0.0980 & 0.0000 \\ -0.1446 & -0.0153 & 0.0752 \end{pmatrix}.$$

In addition, let $\hat{t}_{ij}$ and v_{ij} correspond to the entries of the test statistics $\hat{T}$ and V on and below the diagonal (since the test statistics $\hat{T}$ and V are lower triangular matrices).
In order to test hypothesis 3.9 or hypothesis 3.10 from Osborne et al. (2013), for $\delta = I_3$, we repeatedly resample observations from the original data and compute the generalized Frobenius sample mean for each respective group. The generalized Frobenius sample means are computed as described in Section 2 of Osborne et al. (2013). Figure 1.12 displays a visualization of the bootstrap distributions of the Generalized Frobenius sample means. There, they used 10,000 bootstrap resamples and computed the bootstrap generalized Frobenius sample mean for each respective group.

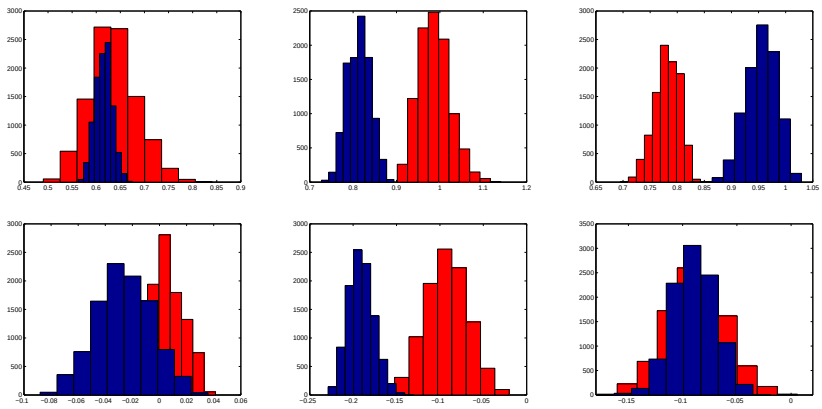

Figure 1.12 Marginals of the bootstrap distribution for the generalized Frobenius sample means for d_{11}, d_{22}, d_{33}, d_{12}, d_{13}, and d_{23}; clinically normal (light red) vs dyslexia (dark blue)

In addition, for each bootstrap resample, we calculate the Cholesky decomposition of the bootstrap generalized Frobenius sample mean for each respective group and then proceed to calculate the bootstrap distribution of our test statistics $\hat{T}$ and V as described in equation 3.16 of Osborne et al. (2013). Figures 1.13 and 1.14 displays a visualization of our non-pivotal bootstrap distribution of our test statistics $\hat{T}$ and V.

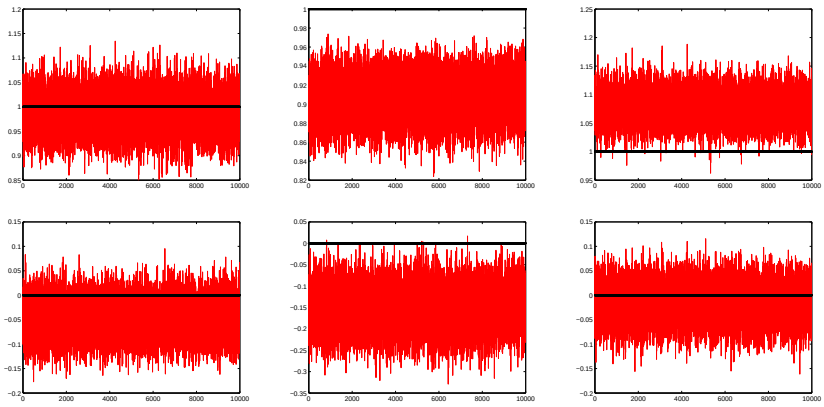

Figure 1.13 Bootstrap distribution of our test statistics $\hat{T}$: The images (1 - 3) in the first row correspond to the diagonal entries of the matrices $\hat{T}^*$: t_{11}, t_{22}, t_{33} and images (4 - 6) in the second row corresponds to the lower triangular off-diagonal entries of the matrices $\hat{T}^*$: t_{21}, t_{31}, t_{32}

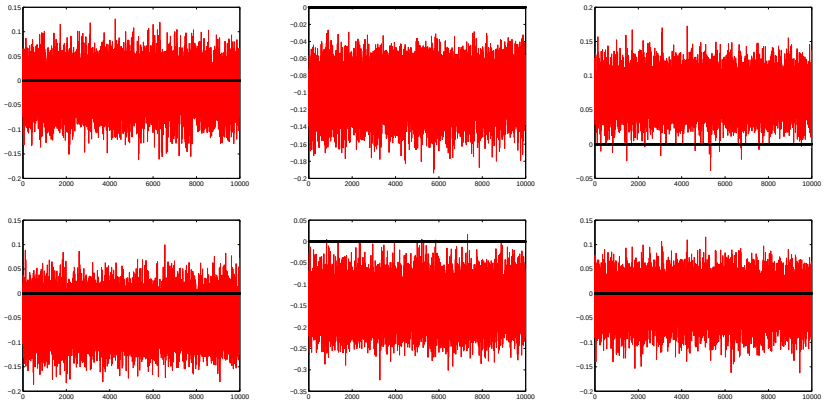

Figure 1.14 Bootstrap distribution of our test statistics V: The images (1 - 3) in the first row correspond to the diagonal entries of the matrices V^*: v_{11}, v_{22}, v_{33} and images (4 - 6) in the second row corresponds to the lower off-diagonal entries of the matrices V^*: v_{21}, v_{31}, v_{32}

Under the null hypothesis 3.10 of Osborne et al. (2013), $\delta = I_3$ on $T^+(3,\mathbb{R})$ or $\log(\delta^{-1}) = \mathbf{0}_3$ on the vector space $T(3,\mathbb{R})$ of lower triangular 3×3 matrices; however, after visually examining Figures 1.13 and 1.14, we informally conclude that there is significant difference between the generalized Frobenius means of the clinically normal and dyslexia group, since the $\hat{T}^*_{22}$ and V^*_{22} values do not overlap with $\delta_{22} = 1$, respectively with $\mathbf{0}_{3,22} = 0$. Moreover, we also observed that the distributions of $\hat{T}^*_{33}$, V^*_{33} and $\hat{T}^*_{31}$, V^*_{31} barely touch $\delta_{33} = 1$, $\mathbf{0}_{3,33} = 0$ and $\delta_{31} = 0$, $\mathbf{0}_{3,31} = 0$.

These results are formally confirm at level α, that there is significant evidence that the clinically normal and dyslexia children display on average different DTI responses. The result were obtained by constructing a $100(1-\alpha)\%$ - simultaneous bootstrap confidence intervals, as described in Remark 3.8 of Osborne et al. (2013), for $\hat{T}_{ij}$ and V_{ij}. Tables 2 and 3 in Osborne et al. (2013) display the results of the Bonferroni $100(1-\alpha)\%$-simultaneous bootstrap confidence intervals for $\hat{T}_{ij}$ and V_{ij} at various significance levels: for example the 94% simultaneous c.i. for T_{22} and T_{33} are $(0.8488, 0.9600)$ respectively $(1.0085, 1.1465)$, and the simultaneous c.i. 94% for V_{22} and V_{33} are $(-0.1640 - 0.0409)$ respectively $(0.0084, 0.1367)$, both pointing to a significant mean

difference between the two groups of children.

1.8 MRI data analysis of Corpus Callosum Image

Albert Einstein's brain was removed shortly after his death (most likely without prior family consent), weighed, dissected and photographed by a pathologist. Among other pictures, a digital scan of a picture of the General Relativity creator's half brain taken at the autopsy is displayed below. The *Corpus Callosum* (CC) connects the two cerebral hemispheres and facilitates interhemispheric communication. It is the largest white matter structure in the brain. We extracted the contour of the CC from this Einstein's brain image, the shape of which would be set at the center of a null hypothesis in our testing problem (see Figure 1.15).

Figure 1.15 Right hemisphere of Einstein's brain including CC midsagittal section (left) and its contour (right).

Fletcher (2013) extracted contours of CC midsagittal sections from MRI images, to study possible age related changes in this part of the human brain. His study points out certain age related shape changes in the corpus callosum. Given that Einstein passed away at 76, we consider a subsample of corpus callosum brain contours from Fletcher (2013), in the age group 64-83, to test how far is the average CC contour from Einstein's. The data is displayed in Figure 1.16.

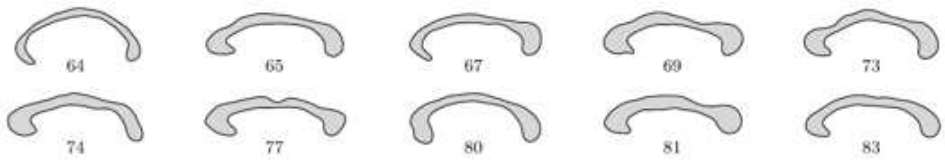

Figure 1.16 Corpus callosum midsagittal sections shape data, in subjects ages - 65 to 83

We consider contours, boundaries of 2D topological disks in the plane. To keep the data analysis stable, and to assign a *unique* labeling, we make the *generic* assumption that across the population there is a unique anatomical or geometrical landmark starting point p_0 on such a contour of perimeter one, so that the label of any other point p on the contour is the 'counterclockwise' travel time at constant speed from p_0 to p. A *regular contour* $\tilde{\gamma}$ is regarded as the range of a piecewise differentiable *regular* arclength parameterized function $\gamma : [0, L] \to \mathbb{C}, \gamma(0) = \gamma(L)$, that is one-to-one on $[0, L)$. Two contours $\tilde{\gamma}_1, \tilde{\gamma}_2$ *have the same direct similarity shape* if there is a direct similarity $S : \mathbb{C} \to \mathbb{C}$, such that $S(\tilde{\gamma}_1) = \tilde{\gamma}_2$. Two regular contours $\tilde{\gamma}_1, \tilde{\gamma}_2$ have the same similarity shape if their centered

counterparts satisfy $\tilde{\gamma}_{2,0} = \lambda\tilde{\gamma}_{1,0}$, for some $\lambda \in \mathbb{C}\backslash 0$. Therefore Σ_2^{reg}, *set of all direct similarity shapes of regular contours,* is a dense and open subset of $P(\mathbf{H})$, the projective space corresponding to the Hilbert space $\mathbf{H}$ of all square integrable centered functions from S^1 to $\mathbb{C}$. (see Ellingson et al. (2013)).

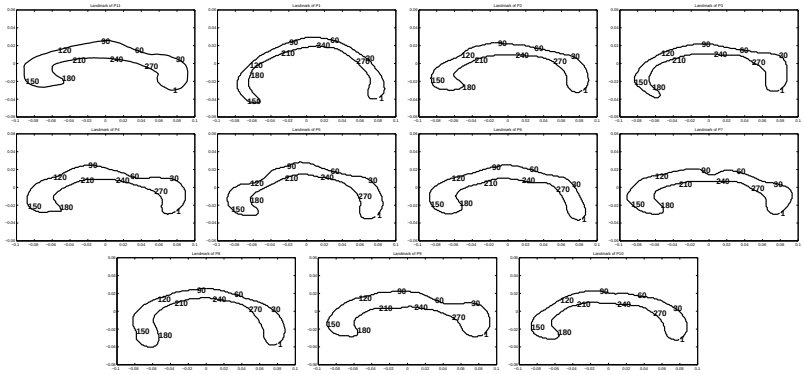

Figure 1.17 Matched sampling points on midsagittal sections in for CC data (Einstein's is the upper left CC).

We will use the neighborhood hypothesis testing method on the manifold of planar contours to test if the average shape of the CC in a population of sixty five to eighty three years old people is close to the shape of Einstein's CC in the sense of Ellingson et al. (2013). Data in Figure 1.16 was used to test the hypothesis that the mean CC shape is in a small ball of radius δ around the shape of Einstein's CC (see Qiu et al. (2014)). Note that Fletcher (2013), from which we borrowed the MRI data, tacitly assumes that the similarity shape is preserved during the data acquisition. Likewise, frontal pinhole camera images of a planar scene are similarity preserving (see Mardia and Patrangenaru (2005)); therefore, comparing similarity shapes from data collected using these two methods makes sense.

The closest representatives of the VW sample mean of the shapes of contours of the CC midsections compared to the shape of Einstein's CC midsection are displayed in Figure 1.18. The overlaps of the two contours are rare, which visually shows that the average CC contour shape is significantly different from Einstein's. The 95% bootstrap confidence region for the extrinsic mean CC contour, based on a conveniently selected icons is given in Figure 1.19.

We set δ as the radius of the null hypothesis ball around Einstein's CC contour shape, as a point p_0 on $P(\mathbf{H})$. The maximum value for δ where the test is significant was found to be 0.1367, which is quite large taking into account the fact that the diameter of any finite dimensional complex projective space with the VW metric, is $\sqrt{2}$. The result is explained by the fact that Einstein's brain halves had more interconnections than in an the average sixty-five to eighty-three years old individual. This is reflected in the thicker shape appearance of his CC midsection; when this shapes are regarded as points on the shape space $P(\mathbf{H})$, p_0 is a remote outlier of the cluster of shapes of CC's in the data due to the fact that these are thinner.

Acknowledgments

The authors acknowledge support from grants NSA-MSP- H98230-14-1-0135 and NSF-DMS-1106935. They are grateful to the referee for helpful comments that significantly improved the manuscript, and to E. R. Reisch (LSU) for providing the CT data.

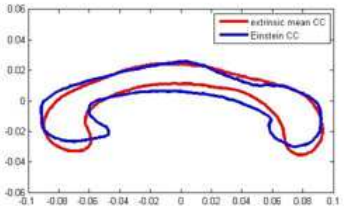

Figure 1.18 Registered icons for 2D direct similarity shapes of CC midsections : sample mean (light red) vs Albert Einstein's (dark blue)

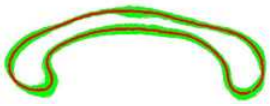

Figure 1.19 95% bootstrap confidence region for the extrinsic mean CC contour by 1000 resamples.

INDEX

References

Appleton B and Talbot H 2006 Globally minimal surfaces by continuous maxial flows. *IEEE Trans. Pattern Ana. and Mach. Intell.* **28**(1), 106–118.

Bandulasiri A and Patrangenaru V 2005 Algorithms for nonparametric inference on shape manifolds. *Proceedings of the Joint Statistical Meetings 2005* pp. 1617–1622.

Bandulasiri A, Bhattacharya R and Patrangenaru V 2009 Nonparametric inference for extrinsic means on size-and-(reflection)-shape manifolds with applications in medical imaging. *Journal of Multivariate Analysis* **100**, 1867–1882.

Bhattacharya R and Patrangenaru V 2003 Large sample theory of intrinsic and extrinsic sample means on manifolds-part I. *Annals of Statistics* **31, no. 1**, 1–29.

Bhattacharya R and Patrangenaru V 2005 Large sample theory of intrinsic and extrinsic sample means on manifolds-part II. *Annals of Statistics* **33, no. 3**, 1211–1245.

Bookstein F 1991 *Morphometric Tools for Landmark Data, Geometry and Biology*. Cambridge University Press, Cambridge.

Bresson X, Esedoglu S, Vandergheynst P, Thiran J and Osher S 2005 Global minimizers of the active contour/snake model.. *In FBP: Theory and Applications*.

Burgoyne C, Thompson HW, Mercante DE and Amin R 2000 *The Shape of Glaucoma, Quantitative Neural Imaging Techniques* Kugler Publications, The Hague, The Netherlands. Eds: H. G. Lemji and J. S. Schuman chapter Basic Issues in the Sensitive and Specific Detection of Optic Nerve Head Surface Change Within Longitudinal LDT TOPSS Images, pp. 1–37.

Cabra lB, Cam N and Foran J 1994 Accelerated volume rendering and tomographic reconstruction using texture mapping hardware. *Proceedings of ACM/IEEE Symposium on Volume Visualization* pp. 91–98.

Caselles V, Kimmel R and Sapiro G 1997 Geodesic active contours. *Intl. Journ. of Computer Vision* **22**(1), 61–79.

Crane M and Patrangenaru V 2011 Random change on a Lie group and mean glaucomatous projective shape change detection from stereo pair images. *Journal of Multivariate Analysis* **102**, 225–237.

Derado G, Mardia K, Patrangenaru V and Thompson HW 2004 A shape based glaucoma index for tomographic images. *Journal of Applied Statistics* **31**, 1241 – 1248.

Drebin R, Carpenter L and Harrahan P 1988 Volume rendering. *SIGGRAPH 88* pp. 665–674.

Dryden I and Mardia K 1998 *Statistical Shape Analysis*. Wiley: Chichester.

Dryden IL, Koloydenko A and Zhou D 2009 Non-Euclidean statistics for covariance matrices, with applications to diffusion tensor imaging. *Ann. Appl. Stat.* **3**(3), 1102–1123.

Dryden IL, Kume A, Lee H and Wood ATA 2008 A multi-dimensional scaling approach to shape analysis. *Biometrika* **95**(4), 779–798.

Efron B 1982 *The Jackknife, the Bootstrap and Other Resampling Plans*. SIAM, Philadelphia.

Ellingson L, Patrangenaru V and Ruymgaart F 2013 Nonparametric estimation of means on Hilbert manifolds and extrinsic analysis of mean shapes of contours. *Journal of Multivariate Analysis* **122**, 317–333.

Faugeras O 1992 What can be seen in three dimensions with an uncalibrated stereo rig?. *Proc. European Conference on Computer Vision, LNCS 588* pp. 563–578.

Fletcher TP 2013 Geodesic regression and the theory of least squares on riemannian manifolds. *Int. J. Comput. Vis.* **105**, 171–185.

Fréchet M 1948 Les elements aleatoires de nature quelconque dans un espace distancie (in French). *Ann. Inst. H. Poincare* **10**, 215–310.

Gibson S, Fyock C, Grimson E, Kanade T, Kikinis R, Lauer H, McKenzie N, Mor A, Nakajima S, Ohkami H, Osborne R, Samosky J and Sawada A 1998 Volumetric object modeling for surgical simulation. *Medical Image Analysis* **2**(2), 121–132.

Harris L and Camp J 1984 Display and analysis of tomographic volumetric images utilizing a vari-focal mirror. *Proceedings of SPIE* **507**, 38–45.

Hartley R and Zisserman A 2004 *Multiple view Geometry in computer vision; 2nd edition*. Cambridge University Press.

Hartley RI, Gupta R and Chang T 1992 Stereo from uncalibrated cameras. *Proceedings IEEE Conference on Computer Vision and Pattern Recognition* pp. 761 – 764.

Hawker MJ, Vernon S, Tattersall CL and Dua HS 2007 Linear regression modeling of rim area to discriminate between normal and glaucomatous optic nerve heads: the bridlington eye assessment project.. *Glaucoma* **16**, 345 – 351.

Heffernan P and Robb R 1985 A new method of shaded surfaced displayed of biological and medical images. *IEEE Trans. Med. Imag* **4**, 26–38.

Herman G and Liu H 1977 Display of three-dimensional information in computed tomography. *JCAT* **1**, 155–160.

Kass M, Witkin A and Terzopoulos D 1988 Snakes: Active contour models. *Intl. Journ. of Computer Vision* **1**(4), 321–331.

Kaufman A, Cohen D and Yagel R 1993 Volume graphics. *IEEE Computer* **26**(7), 51–64.

Kendall D 1984 Shape manifolds, Procrustean metrics, and complex projective spaces. *Bull. London Math. Soc.* **16**, 81–121.

Kendall D, Barden D, Carne T and Le H 1999 *Shape and Shape Theory*. Wiley, New York.

Kent JT 1994 The complex Bingham distribution.. *J. Roy. Statist. Soc. Ser. B* **56**, 285–299.

Kent JT and Mardia KV 2012 A geometric approach to projective shape and the cross ratio. *Biometrika* **99**, 833–849.

Levoy M 1988 Display of surfaces from volume data. *IEEE Computer Graphics and Applications* **8**(5), 29–37.

Lorensen W and Cline H 1987 Matching cubes: A high-resolution 3-D surface construction algorithm. *Computer Graphics* **21**(3), 163–169.

Ma Y, Soatto S, Košecká S and Sastry SS 2006 *An Invitation to 3-D Vision*. Springer.

Mardia KV and Patrangenaru V 2005 Directions and projective shapes. *Ann. Statist.* **33**, 1666–1699.

Mardia KV, Kent JT and Bibby JM 1979 *Multivariate Analysis*. Academic Press.

Milnor J 1963 *Morse Theory*. Princeton University Press.

Osborne D, Patrangenaru V, Ellingson L, Groisser D and Schwartzman A 2013 Nonparametric two-sample tests on homogeneous Riemannian manifolds, Cholesky decompositions and diffusion tensor image analysis. *Journal of Multivariate Analysis* **119**, 163–175.

Osborne DE 2012 Nonparametric data analysis on manifolds with applications in medical imaging. *Electronic Theses, Treatises and Dissertations. Paper 5085. http://diginole.lib.fsu.edu/etd/5085*.

Patrangenaru V, Liu X and Sugathadasa S 2010 Nonparametric 3D projective shape estimation from pairs of 2d images - I, in Memory of W.P. Dayawansa. *Journal of Multivariate Analysis* **101**, 11–31.

Patrangenaru V, Thompson H and Derado G 2000 Large sample and bootstrap methods on for 3D shape change with applications to detection of glaucomatous change in images of the optic nerve head. *Abstracts of the Leeds Annual Statistics Research Workshop in honor of the 65th birthday of Professor K.V.Mardia,*
http://www.maths.leeds.ac.uk/Statistics/workshop/leeds2000 pp. 30–33.

Pflesser B, Tiede U and Hohne K 1998 Specification, modelling and visualization of arbitrarily shaped cut surfaces in the volume model. *Medical Image Computing and Computer-Assisted Intervention-MICCAI* **1496**, 853–860.

Qiu M, Patrangenaru V and Ellingson L 2014 How far is the corpus callosum of an average individual from albert einstein's? *Proceedings of COMPSTAT-2014, The 21st International Conference on Computational Statistics*, pp. 403–410, Geneva.

Robb R 1994 *Three-Dimensional Biomedical Imaging-Principle and Practice*. VCH Publishers, New York.

Robb R 1996 *Visualization methods for analysis of multimodality images. In: Functional Neroimaging: Technical Foundations*. Academics Press, San Diego.

Robb R and Barillot C 1989 Interactive display and analysis of 3-d medical images. *IEEE Trans. Med. Imag.* **8**(3), 217–226.

Sanfilippo PG, Cardini A, Hewitt AW, Crowston JG and Mackey DA 2009 Optic disc morphology–rethinking shape. *Progress in Retinal and Eye Research* **28**(4), 227–248.

Schwartzman A, Dougherty RF and Taylor JE 2008 False discovery rate analysis of brain diffusion direction maps. *Annals of Applied Statistics* **2**, 153–175.

Serra L, Nowinsk W, Poston T, Hern N, Meng L, Guan C and Pillay P 1997 The brain bench: Virtual tools for stereotactic frame neurosurgery. *Medical Image Analysis* **1**(4), 317–329.

Sher L 1977 Graphics in space: See it now. *Proceedings of NCGA* **3**, 101–160.

Sughatadasa SM 2006 Affine and projective shape analysis with applications. *Ph.D. Dissertation, Texas Tech University*.

Unger M, Pock T, Trobin W, Cremers D and Bischof H 2008 Tvseg - interactive total variation based image segmentation. *Proceedings of the British Machine Vision Conference (BMVC)*.

Ziezold H 1977 On expected figures and a strong law of large numbers for random elements in quasi-metric spaces.. *Transactions of the seventh Prague conference on information theory, statistical decision functions, random processes and of the eighth European meeting of statisticians, Reidel, Dordrecht* pp. 591–602.